J. Fluid Mech. (1989), *vol.* 204, *pp.* 479–500
Printed in Great Britain

Vertical mixing due to the breaking of critical internal waves on sloping boundaries

By G. N. IVEY† AND R. I. NOKES‡
Research School of Earth Sciences, Australian National University, GPO Box 4, Canberra, A.C.T., 2601, Australia

(Received 8 October 1987 and in revised form 23 January 1989)

A laboratory experiment is used to examine the vertical mixing resulting from the breaking of internal waves on a sloping boundary in a continuously stratified fluid. Attention is confined to the case of critical waves when the slope of the group velocity vector of the incident waves is equal to the bottom slope. Along the sloping boundary a turbulent bottom boundary layer forms with a thickness dependent on the incident wave amplitude. The mixing efficiency, defined as the ratio of the increase in potential energy due to mixing to the loss of kinetic energy by the incident waves, is dependent upon the stability of the flow and has an upper bound of approximately 0.20.

By examining the increase in potential energy of the fluid as a result of sustained mixing, we are able to compute the transition value of the dissipation ϵ_{tr} below which no mixing occures. For mixing due to the breaking of critical internal waves on sloping boundaries we find that $\epsilon_{tr} = (8 \pm 2)\nu N^2$. From comparisons with experiments with grid-generated turbulence, this suggests that while $\epsilon_{tr}/\nu N^2 = O(10)$ in the available data sets, the specific value of ϵ_{tr} may be mechanism dependent.

1. Introduction

The oceanic internal wave field contains significant amounts of energy and thus provides a potentially important energy source for driving mixing in the density stratified ocean. In this study we are concerned with the mixing that can occur in any stratified water body when internal waves interact with solid sloping boundaries. On the oceanic continental shelves the mixing driven by breaking internal waves may be significant for the overall dynamics (Baines 1986). In the deep ocean, recent work (Eriksen 1985; Garrett & Gilbert 1988) has explored the possibility that internal waves breaking near the sloping boundaries may produce significant amounts of vertical, or diapycnal, mixing when averaged over the entire ocean basin.

Diapycnal mixing rates in the deep ocean have occasionally been inferred from fitting observed property distributions to some form of steady state advective–diffusive balance. For example, Munk (1966) assumed a balance between vertical diffusion and vertical advection and used vertical profiles of temperature, salinity and Carbon-14 from the Pacific to obtain a diapycnal eddy diffusivity of 1.3×10^{-4} $m^2 s^{-1}$. Hogg *et al.* (1982) assumed a balance between the vertical diffusion of heat and the vertical advection of heat for the near-bottom water in the Brazil Basin in the South Atlantic to estimate a diapycnal eddy diffusivity of $3\text{–}4 \times 10^{-4}$ $m^2 s^{-1}$.

† Current address: Centre for Water Research, University of Western Australia, Nedlands, Western Australia, 6009.

‡ Current address: Theoretical and Applied Mechanics, University of Auckland, Auckland, New Zealand.

Saunders (1987) assumed a balance between the vertical diffusion of heat and the horizontal flux of heat, associated with the flow through Discovery Gap onto the Iberian Abyssal Plain in the Eastern Atlantic, and estimated an eddy diffusivity for the region north of the Gap as 1.5×10^{-4} m^2 s^{-1}.

While these estimates therefore suggest eddy diffusivities of order 10^{-4} m^2 s^{-1}, possible mixing mechanisms acting in midwater, such as internal wave breaking or double-diffusive instabilities, appear unable to provide sufficiently large mixing rates (Garrett 1979). These estimates require further work, and direct measurements of turbulent microstructure (e.g. Moum & Osborn 1986; Gregg & Sanford 1988) will also assist in providing better estimates of interior eddy diffusivities. In addition to this direct interior mixing, there is also the possibility that energetic mixing at the boundaries followed by advection and stirring into the interior may lead to significant diapycnal mixing over the ocean basin (Munk 1966; Armi 1978; Ivey 1987*a*).

Eriksen (1985) and Garrett & Gilbert (1988) have examined the mixing that can occur when internal waves are reflected off the sloping bottom. In particular, they have shown that after reflection there is an enhancement of the vertical shear and hence the possibility of a shear-flow instability leading to a breaking of the internal waves near the sloping bottom. This shear enhancement is particularly strong for frequencies around the critical frequency $\omega_c = (N^2 \sin^2\theta + f^2 \cos^2\theta)^{\frac{1}{2}}$ (where ω is the wave frequency, θ the angle between the bottom and the horizontal, and N and f the buoyancy and Coriolis frequencies, respectively) when the slope of the group velocity vector is equal to the bottom slope. The authors' have made initial estimates of the amount of energy loss associated with this mechanism, although further work is required to refine these estimates (Garrett & Gilbert 1988).

What is clear from this work is that by a bottom reflection mechanism significant amounts of energy can be provided from the internal wave field for driving mixing near the sloping boundaries. In order to estimate the effective diapycnal transport, one also needs an estimate of the mixing efficiency as only a certain portion of the available energy will ultimately be converted to an increase in potential energy. McEwan (1983) measured mixing efficiencies due to the resonant interaction of waves in the interior of a stratified fluid. For the case of waves impinging on a sloping boundary, Cacchione & Wunsch (1974) demonstrated that an instability can occur for critical conditions, but made no quantitiative estimates of the mixing process. It is the purpose of the present laboratory experiments to study the mixing resulting from the breaking of internal waves on sloping boundaries and to estimate the efficiency of that mixing. This paper concentrates on the case of critical waves incident on a smooth sloping boundary. The experiments are done in a non-rotating reference frame and while the absence of rotation does not change the character of the wave motion, the expression for the critical frequency does simplify to $\omega_c = N \sin\theta$. The mixing driven by subcritical and supercritical waves will be discussed elsewhere.

2. Laboratory experiments

The experiments were conducted in a tank 4.22 m long, 40 cm high and 20 cm wide. It consisted of three coupled sections: two 2 m long sections of glass connected by a 22 cm long central section fabricated from acrylic sheet in which a plane paddle wave maker was centrally mounted. At the far end of each of the glass sections acrylic sheets were installed at an angle of $\theta = 30°$ to the horizontal to form sloping bottoms. The two bottom slopes were installed parallel to one another to create a

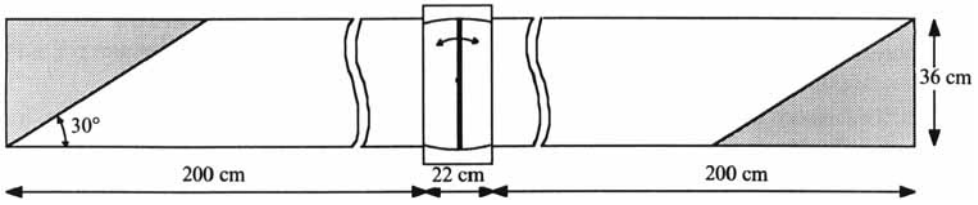

FIGURE 1. Schematic of the laboratory tank.

large parallelogram-shaped working section with the paddle in the middle of the tank (figure 1). The horizontal cross-sectional area of the tank was independent of height and this enabled the working section to be filled with an accurate linear stratification by the two-tank technique (Fortuin 1960), using salt as the stratifying medium. Moreover, the symmetry of the whole tank about the centrally located paddle ensured that mixing occurred equally in each half of the tank, thus avoiding the problems in quantifying the overall mixing that could occur if the paddle was located at one end of the tank.

The paddle itself was mounted on two Teflon studs, 3 mm in length and diameter, projecting horizontally through the tank walls at midheight in the central box section. The paddle was free to pivot about its central horizontal axis and carefully aligned with a clearance between the paddle and vertical sidewalls of approximately 0.5 mm. To accommodate the swing of the paddle, shallow recesses were machined into the 1 cm thick acrylic sheet which formed the top and bottom of the central section and the clearance between recess and paddle was also about 0.5 mm. The central box section was then bolted to the glass sections. As the tank was filling, 1 cm thick styrofoam sheets covering the entire water surface were added to prevent any near-surface mixing due to air movement in the laboratory. After the completion of filling, the sheets were fixed in position by taping them against the tank sidewalls and the final working depth of fluid in the tank was 36 cm (figure 1).

An eccentric crank and driving-arm mechanism was used to drive the paddle in a sinusoidal motion and the paddle amplitude was kept constant for a given run. The paddle was connected to the driving arm via a sensitive $\pm 0.5\,N$ force transducer mounted so that it measured the applied force perpendicular to the paddle throughout its swing. The product of the measured force and the paddle displacement enabled the computation of the work done by the paddle on the fluid (§4.2). The amount of mixing was determined by measuring density profiles with a four-wire microconductivity probe. In practice, measurements were made with the fluid quiescent both before and after a measured number of wave cycles and this enabled the computation of the increase in potential energy of the system. The ratio of this increase in potential energy to the work done by the paddle (i.e. the input kinetic energy) yielded a measure of the mixing efficiency of the system (§4.2). In addition, velocity measurements were made by tracking neutrally buoyant particles and a rainbow colour schlieren technique was used for flow visualization as described in the next section.

3. Flow visualization

The rainbow schlieren technique introduced by Howes (1984, 1985) was employed to examine the breaking of the waves on the sloping bottom. Rainbow schlieren differs from conventional colour schlieren in that the usual knife-edge or colour strip is replaced by a radial rainbow filter. The rainbow technique accentuates detail far

more than ordinary schlieren and while the performance is comparable to that of Mach–Zendler interferometry, it is much simpler, cheaper and easier to use for large-scale visualization (Howes 1985).

The filters used in the experiments were produced by: (1) passing white light through a 45° glass prism to separate the colours and exposing the resulting linear rainbow onto 10.2 cm × 12.7 cm Ektachrome tungsten sheet film; (2) the entire rainbow was then masked off with the exception of a thin slit down the centre; and (3) the masked film was then placed in an enlarger and the image projected vertically down onto a second sheet of film placed in a film holder and spun in a horizontal plane with the aid of a small electric motor. The net effect was to produce a radially symmetric bull's-eye or rainbow filter of approximately 6.5 cm in diameter. This master rainbow was then duplicated onto 35 mm Ektachrome film and mounted in a slide holder. While the final size of the bull's-eye and direction of the colour spectrum could be varied, the most effective configuration for the present experiments was a bull's-eye with a 2 cm outside diameter and a colour spectrum ranging from either a white or blue centre through to red on the outside against a black background.

For the experiments, the filter was mounted in a holder at the focal point of a 25 cm diameter front-silvered concave schlieren mirror of focal length 244 cm. A 150 W slide projector, with the front lens removed, was used to back illuminate the rainbow filter. Back illumination of this filter then produced diverging light rays which were projected onto the concave schlieren mirror and reflected off with an included angle of about 5° between the centre of the incident and reflected beams from the mirror. The reflected light beam, with now parallel light rays, then passed horizontally through the side of the tank and onto a second, identical schlieren mirror. The two mirrors were 5.38 m apart and the 20 cm wide tank was placed at the midpoint of this gap. The light beam then reflected off the second mirror and the included angle between incident and reflected beams was again about 5°. The reflected beam, with now convergent light rays, was then focused onto a flat plate placed perpendicular to the centreline of the reflected beam and exactly at the focal point of the second mirror (244 cm). The net effect was that a 2 cm diameter image of the original 2 cm diameter rainbow filter was re-formed on this plate. A 2 mm diameter pinhole in the centre of the plate allowed light to pass through to the camera on the other side of the plate. The entire light/filter to mirror to mirror to pinhole/camera system thus formed a z-configuration with 5° included angles.

The system was arranged such that at rest only one colour, usually the central colour of the filter, was allowed to pass through the pinhole and into the camera. This colour then corresponded to the initial density gradient in the tank. Any disturbances in the flow field then allowed other colours through the pinhole. Owing to the circular symmetry, equal changes of the density gradient above or below the initial gradient can produce the same colour, but this disadvantage is more than outweighed by the enhanced sensitivity of the system owing to its response to variation in density gradient in all directions and, hence, in visualizing turbulent mixing events. In particular, as shown below, turbulent mixing patches blended the individual colours in the spectrum to produce whitish patches (since we do not have a perfect spectrum in the filter) which were then clearly distinguishable from the laminar, coloured surrounding fluid in the schlieren images. Either a video or a still camera fitted with a zoom lens was used to record the schlieren images.

(a)

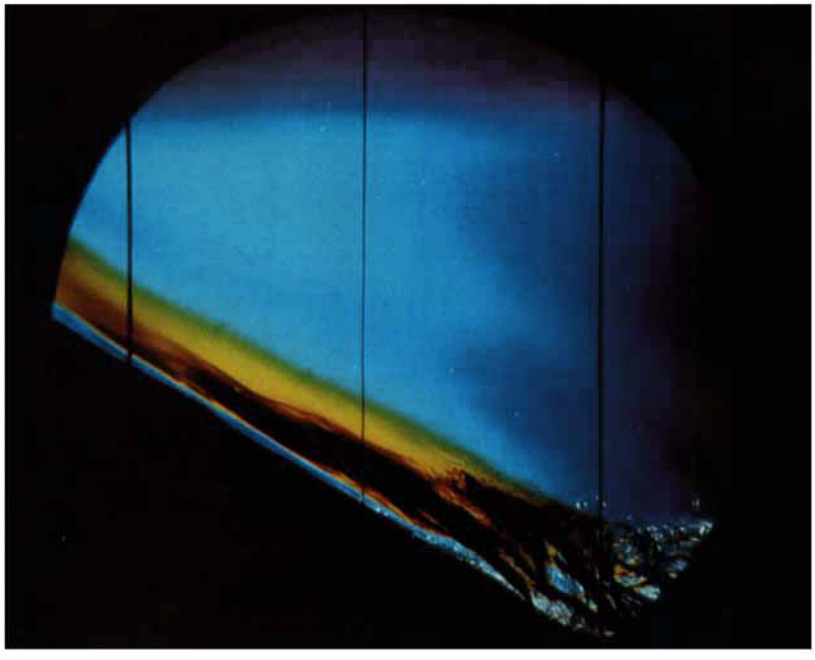

(b)

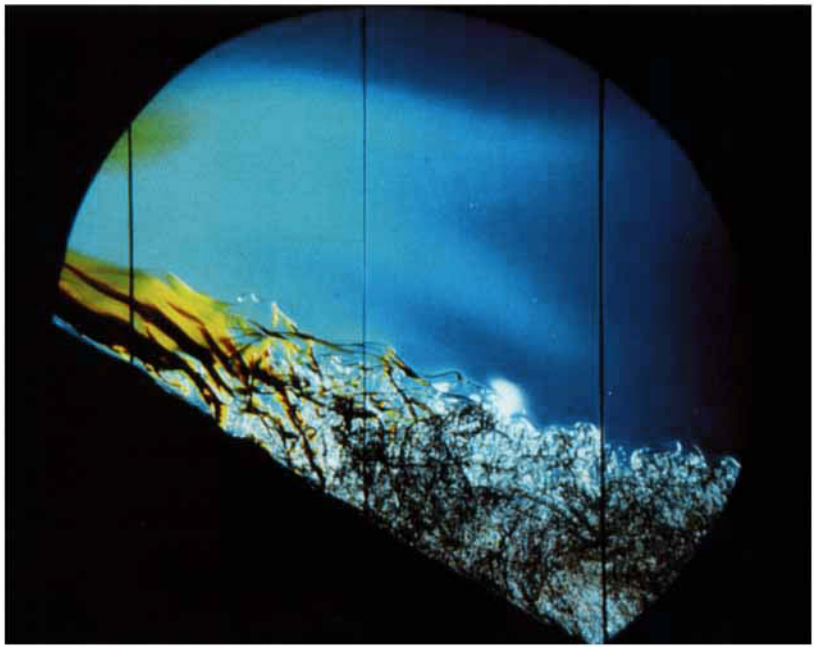

 FIGURE 2 (*a, b*). For caption see overleaf. (*Facing p.* 482)

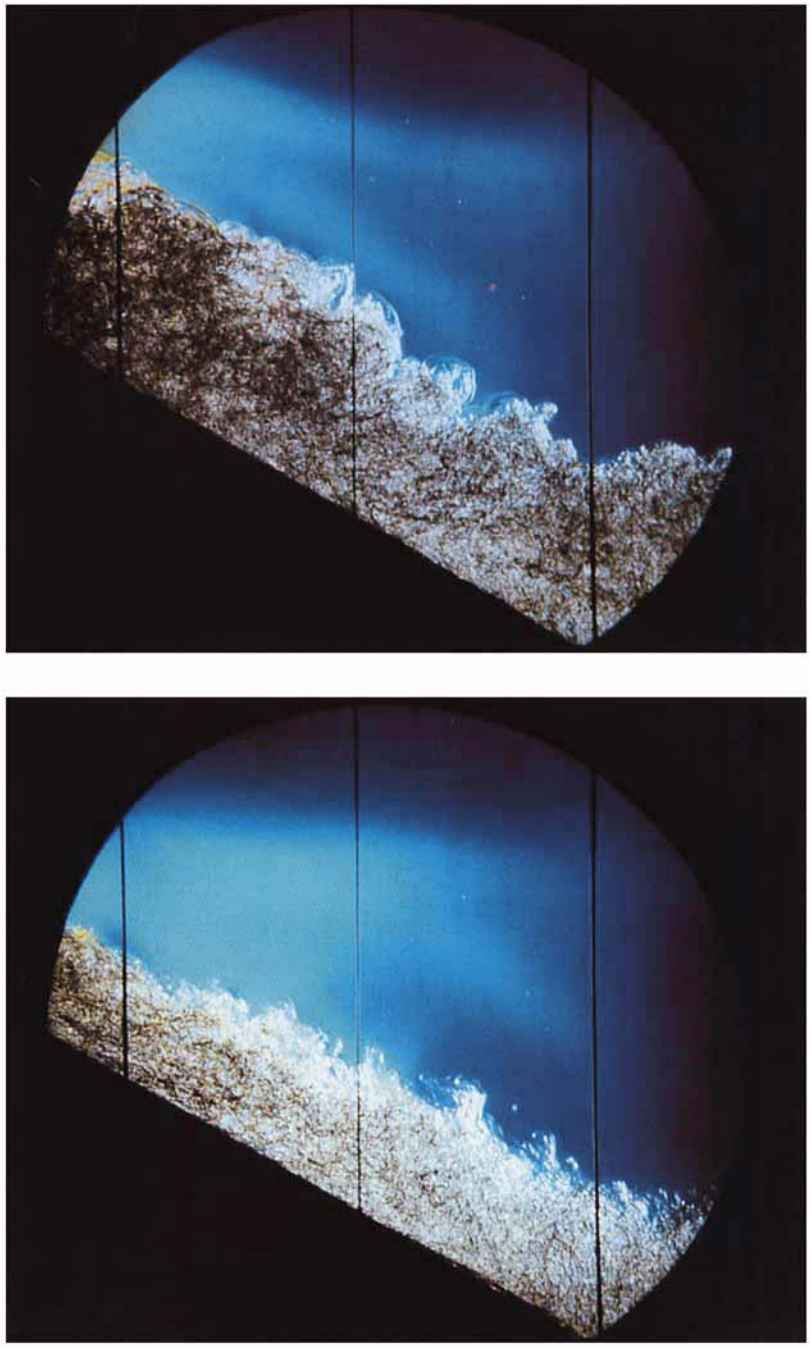

FIGURE 2. Time sequence of photos for a run with buoyancy frequency N=0.60rs^{-1}, wave frequency ω=0.30rs^{-1} and paddle amplitude A=4.6 cm. The photos were taken at *(a)* 3.44, *(b)* 4.20, *(c)* 4.54 and *(d)* 4.82 wave periods after the commencement of paddle motion. The paddle is to the right in the photographs and the vertical scale lines are 10 cm apart.

4. Results

4.1. *Boundary-layer structure on the sloping bottom and description of the flow*

The schlieren mirrors were set up at midheight on the sloping bottom with the centre of the observation point 180 cm from the paddle (see figure 1). Figures 2 (plates 1 and 2) and 3 show typical time sequences following the commencement of paddle motion (note that in all photographs the paddle was to the right of the field of view and the waves were thus propagating from right to left). In these figures, the rainbow filter had a white core and the system was aligned slightly off-centre so that the initial background stratification corresponded to dark blue. With a bottom slope of $\theta = 30°$, critical conditions occurred when the wave frequency $\omega_c = \sin\theta N = 0.5N$. For the conditions prevailing in figure 2 and 3, it took about 0.5 wave periods after the commencement of paddle motion before a wave travelling at the group velocity with the fundamental mode (§4.2) arrived at the observation point. Neutrally buoyant beads placed in the flow above the slope did indeed start to oscillate after this timescale (see below). The strength of this oscillatory motion steadily increased until after two or three cycles of the paddle the schlieren indicated a strong surge up the slope. During the upslope phase of motion, the structure was laminar, although there were large refractive-index variations (through to black for extreme gradients) associated with the motion. During the downslope phase, the structure remained laminar although there was some suggestion of instability in a thin boundary layer (of less than 0.5 cm in thickness) on the bottom.

This picture changed rapidly with the arrival of the next wave when the upslope flow resembled an advancing turbulent bore (figure 2*a–c*) with strong billowing motion and intense small-scale structure within the entire region behind the nose (with a thickness of around 8 cm in figure 2*c*, for example). This bore decelerated as it approached the apex of the wedge at the top of the slope. As the flow on the slope reversed, the boundary-layer thickness decreased although it still remained active with overturning on small scales (recall the forcing frequency $\omega_c = 0.5\,N$). The arrival of the next wave was heralded by another turbulent bore advancing up the slope into the turbulent field adjacent to the bottom left by the previous surge. The net effect was to produce a turbulent bottom boundary layer along the bottom slope (figure 2*d*) in about 4 wave cycles. For distances of the order of the boundary-layer thickness down the slope from the apex of the wedge there appeared to be a reduction in the strength of the flow and a suggestion of slightly weaker mixing although this could not be detected in the observed change in the density profiles (§4.2).

The Reynolds number for this advancing bore (based on the speed of advance and thickness of the bore) varied between approximately 1×10^3 and 3.5×10^3 for various runs depending on incident wave amplitude. A feature very evident from the videotapes was the tendency for the mixing to be more energetic for upslope motions than for the subsequent downslope motions. On occasion, there was a tendency for a series of backward-breaking rollers to form behind the advancing nose (e.g. figure 3*a–c*). In figure 3(*b*) these rollers had a thickness of some 8 cm – comparable with the final steady-state boundary-layer thickness. With the arrival of the next wave, these initial instabilities coalesced and a turbulent bottom boundary layer again formed along the bottom slope (figure3*d*). While these structures were interesting, they were very short-lived and were only rarely observed – figure 2, for example, was much more typical.

When the wave amplitude was reduced, the initial motion, two or three wave periods after the start of paddle motion, was again a surge along the bottom slope.

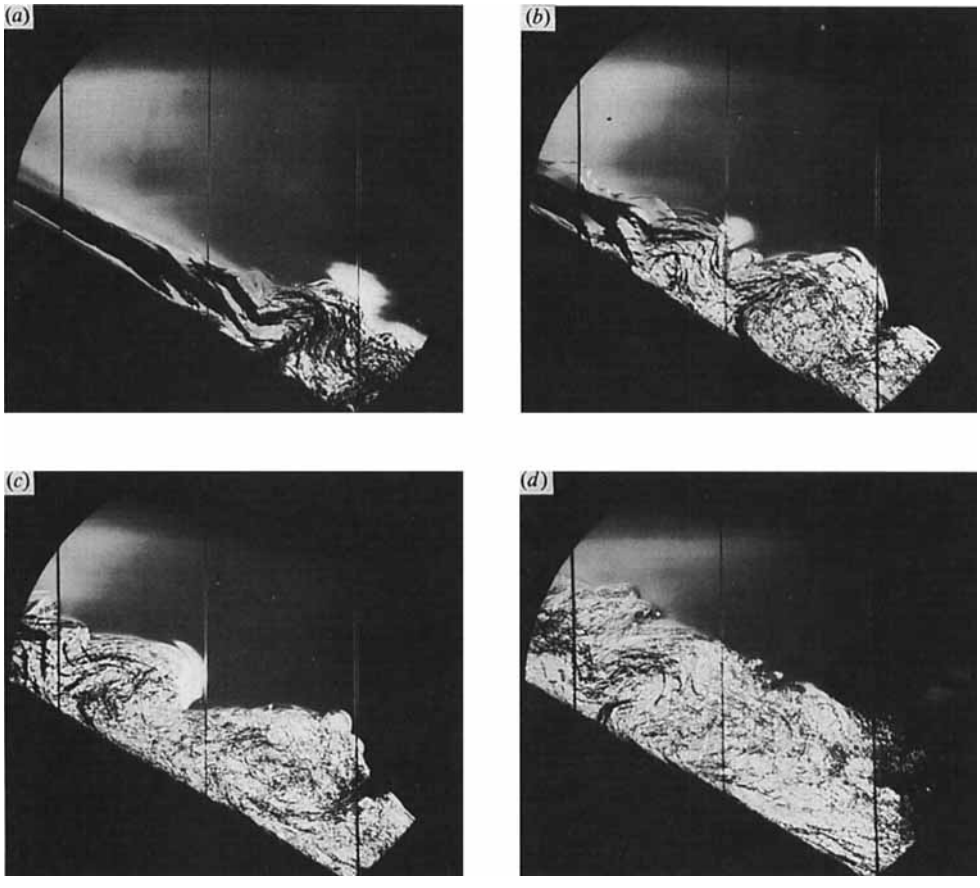

FIGURE 3. Time sequence of photos for a run with buoyancy frequency $N = 0.60\ \mathrm{rs}^{-1}$, wave frequency $\omega = 0.30\ \mathrm{rs}^{-1}$ and paddle amplitude $A = 3.68$ cm. The photos are taken at (*a*) 4.06, (*b*) 4.15, (*c*) 4.30 and (*d*) 5.25 wave periods after the commencement of paddle motion. Vertical scale lines are 10 cm apart.

In this case, however, the laminar surging motion did not break down into a chaotic turbulent motion with the arrival of successive waves. From video tapes of the schlieren images it was possible to characterize the various runs by a Reynolds number $Re = \omega\zeta^2/\nu$, where ω is the wave frequency and ζ the wave amplitude at the paddle (defined in (8) below). Below a critical value of Re in the range 15–20, the schlieren images indicated that turbulent mixing, as evidenced by the appearance of patches of white in the images, were either not persistent over the wave cycle or, at very low values of Re, were not observed at all. Based on these visual observations, we conclude the Reynolds number must exceed 15–20 before a turbulent bottom boundary layer formed. A more precise criterion for transition to a turbulent flow with an observed non-zero buoyancy flux is discussed in §5.

In their laboratory study of breaking waves on bottom slopes, Cacchione & Wunsch (1974) observed regular well-defined vortices on the slope. These structures were not seen either in the observations reported by Thorpe & Haines (1987) or in the present study. One possible explanation of the differences in the three experiments might be sidewall effects. In fact, all three experiments were conducted in tanks with similar widths of about 20 cm. Nevertheless, we conducted some dye studies by using

a syringe to introduce a thin patch of neutrally buoyant dye at the bottom and across the full width of the tank at midheight on the slope prior to the start of a run. When the run was started, we observed that this dye patch was first moved up and down the slope by the initial laminar surge, then when the turbulent bore propagated up the slope, the dye was mixed rapidly over the depth of the bore and uniformly over the width of the tank. There was no indication that the turbulence was initiated or dominated by sidewall effects either at this initial stage or with subsequent mixing. The experiments do differ, however, in the typical Reynolds numbers of the observed flows: in the experiments of Cacchione & Wunsch (1974) $Re \approx 2$, in the experiments of Thorpe & Haines (1987) $Re \approx 20$, and in the present experiments Re was as high as 170. This suggests that the early experiments of Cacchione & Wunsch (1974) most likely differ from the later studies because their Reynolds number was below the transitional value of 15–20 suggested above.

The turbulent bottom-boundary-layer thickness δ was a quantity of some interest. The thickness of this boundary layer varies with the wave period – with a maximum during the upslope phase and a minimum during the downslope phase. While the intensity of the overturning motion appears greatest during the upslope phase, there were persistent small-scale overturning motion over the entire wave cycle. Occasionally, there were intermittent small-scale intrusions which collapsed back into the interior from this boundary layer, although they were not very prominent or persistent even at the largest amplitudes – as also observed in the grid stirring experiments of Phillips, Shyu & Salmun (1986) on sloping boundaries. There was no evidence of any overturning motion remote from the bottom boundary layer. Traverses into the boundary layer with a conductivity probe in conjuction with videotaping of the schlieren images confirmed this observation, and indicated that the bottom boundary layer was not well mixed but rather had a continous density profile essentially the same as the background gradient (within $\pm 10\%$ of the background value of N) only now with small-scale instabilities present.

The turbulent BBL thickness δ was determined from videotapes of the schlieren images, where δ was taken as the distance perpendicular to the slope to the edge of the white region on the schlieren images. The mean value of δ and the maximum deviation $\Delta\delta$ about this mean during one period were determined, and estimates were made both over several wave periods and at four locations along the slope. Once the boundary layer had formed δ, and $\Delta\delta$, were constant along the slope. The resulting estimates for δ and $\Delta\delta$ are shown in figures 4(*a*) and 4(*b*) where the error bars represent $\pm$ one standard deviation. While all the estimates in figure 4 are for critical waves, the buoyancy frequency varied between 0.59 and 1.18 r s^{-1}. To the accuracy of measurement, the data indicate that the boundary-layer thickness δ is a function only of incident wave amplitude ζ and a useful approximation figures 4(*a*) and 4(*b*) is that

$$\delta \approx (5 \pm 1)\,\zeta, \tag{1}$$

where the variation in (1) represents the fluctuation about the mean during one wave period.

Speed measurements in the boundary-layer region were made by tracking neutrally buoyant polystyrene beads. Particles with diameters in the range 0.3–0.4 mm were placed into the fluid and illuminated with a vertical sheet of light about 1 cm wide down the centre of the tank. The particle motions at a position midway along the slope were recorded with a video camera fitted with a zoom lens and the video tapes subsequently analysed to determine speeds. The average speed over one wave period U_{m} was computed for a number of different paddle amplitudes A (defined

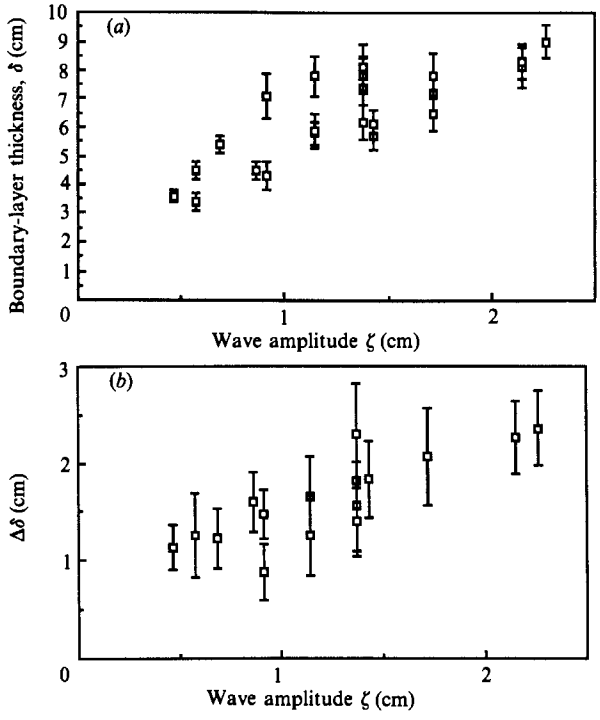

FIGURE 4. (*a*) Turbulent bottom-boundary-layer thickness δ as a function of wave amplitude ζ. A least-squares fit to the data is $\delta = 2.57\zeta + 3.5$ ($r^2 = 0.69$). (*b*) Variation in bottom-boundary-layer thickness $\Delta\delta$ within one wave cycle as a function of wave amplitude ζ.

in (2)) below, and typical profiles for fully established flow (taken as times greater than four wave periods after the commencement of paddle motion) are shown in figure 5(*a*).

The speed in figure 5(*a*) was measured parallel to the slope, and the y-coordinate was normal to the slope. The data indicated a strongly sheared speed profile with the peak in the profile for both data sets in figure 5(*a*) occurring very close to the bottom boundary, and a gradual decay of the velocity with increasing height above the bottom. By comparison, the boundary-layer thickness δ computed from (1) was 6.9 cm and 2.6 cm for the respective runs, and thus the peak in the speed profile occurred in the bottom 10–20% of the boundary-layer thickness. The data also indicate a strong dependence of the magnitude of this peak speed in the boundary layer U_p on paddle amplitude and these peak speeds for runs with varying frequency ω and amplitude A are plotted in figure 5(*b*).

Figure 6 shows a dye study which illustrated the mechanism whereby the sustained mixing in this bottom layer weakened the linear density gradient in the laminar interior. Neutrally buoyant dye was injected through a syringe at about mid-depth in the tank at a point in the boundary layer 150 cm from the paddle and about 1 cm off the sloping bottom. Dye was slowly and steadily injected into the flow, commencing at $t = 7.54T$ and terminating at $t = 10.79T$ (where T is wave period) when the photograph in figure 6(*a*) was taken. The strong alongslope motions in the boundary layer have already mixed the dye a distance of some 30 cm along the slope. The dye has not only been mixed across the thickness of the turbulent bottom boundary layer (some 8 cm thick according to the data in figure

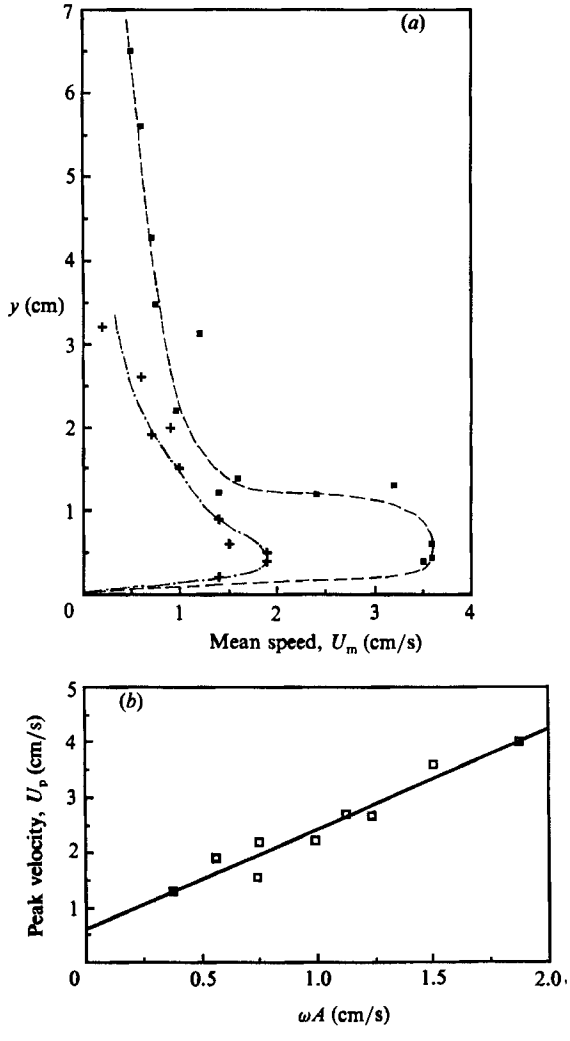

FIGURE 5. (*a*) Average speed over one wave period U_m versus normal distance from the slope y with frequency $\omega = 0.51$ rs^{-1} and paddle amplitudes A of 2.94 cm (■) and 1.10 cm (+). The dashed and dotted lines are drawn by eye. (*b*) Peak speeds U_p in the average speed profile versus ωA. The best-fit straight line shown is $U_p = 1.82\,\omega A + 0.61$ ($r^2 = 0.94$).

4*a*), but some of the dyed fluid has already been pumped out beyond the turbulent boundary layer and started to move out horizontally into the laminar interior (figure 6*a*). As time progressed, dye was mixed further along the bottom slope and was pumped out into the interior at the corresponding level (figure 6*b*, *c*). Note that in figure 6(*d*) at $t = 95.24T$, the process has continued until dye was being pumped out over the entire depth except in thin regions adjacent to the horizontal top and bottom boundaries of the tank. In the interior, the dyed-mixed fluid being continually pumped out of the turbulent bottom boundary layer was steadily spreading over the entire tank (figure 6*d*).

The mechanism for driving the circulation was of the same form as described in the grid-stirring experiments of Ivey & Corcos (1982) and Phillips *et al.* (1986). The continual turbulent mixing drove a turbulent density flux along the boundary within

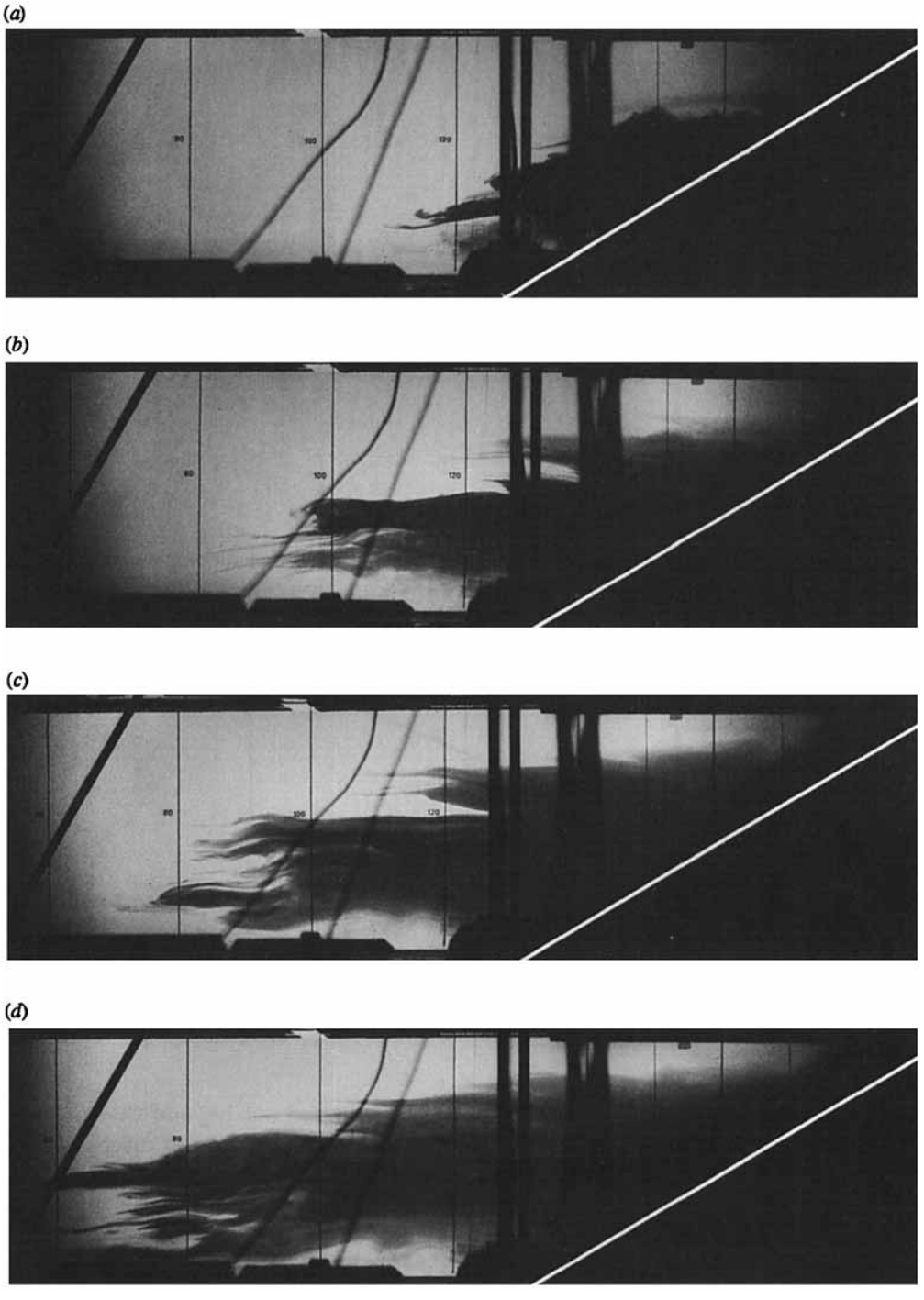

FIGURE 6. Dye injection study showing the overall circulation in the tank (see description in the text). Photographs were taken during continual mixing at (*a*) 10.79, (*b*) 28.49, (*c*) 57.94, (*d*) 95.24 periods after the start of paddle motion. The position of the sloping bottom is marked by the thin diagonal white line.

the turbulent bottom boundary layer and as the fluid column was bounded by top and bottom horizontal boundaries there was a divergence of this along-boundary flux. This, in turn, created a density anomaly between the fluid in the turbulent region and the interior, a slow convergent flow was created in the boundary layer attempting to balance the along-boundary turbulent density flux, and a pumping flow was thus established out of the boundary layer and into the quiescent interior. There was no evidence of persistant small-scale intrusions but rather of a slow cavity-scale circulation with outflow over much of the depth and return flow confined to the relatively thin regions at top and bottom (figure 6). Because the container was bounded, this circulation was closed by a non-zero vertical velocity in the interior and, in particular, it was the vertical divergence of this vertical velocity that caused the interior density gradient to weaken by a stretching of the isopycnals.

The basic requirement for establishing this mechanism is thus a divergence of the turbulent density flux within the boundary layer. In general, this will occur if there are solid horizontal boundaries present, as in the present experiments, if the strength of the mean density gradient varies with distance along the boundary, as is the case in the two-layer grid stirring experiments of Phillips *et al.* (1986), or if the strength of the turbulence varies along the boundary, as one would expect in the ocean. In the ocean rotation is also important and, as Ivey (1987*a*, *b*) has shown in the laboratory, mixed fluid is ejected from the boundary layer by the same mechanism as described above, but is now distributed throughout the cavity not by a coherent cavity-scale circulation but rather by horizontal mixing due to a mesoscale turbulent diffusive mechanism which again leads to a weakening of the interior density gradient.

4.2. *Mixing efficiency*

The continual mixing in the bottom boundary layer on the slope thus led to a slow weakening of the mean density gradient in the tank. The amount of mixing was measured by the changes in vertical profiles of density over the course of an experiment. Density profiles were obtained by traversing a conductivity probe over the depth and converting conductivity to density by calibration against an Anton Paar digital densimeter. Profiles were only taken when the fluid was quiescent and a pair of profiles taken back to back as a check. The procedure was then to oscillate the paddle for a fixed number of wave cycles (usually about 100), stop the paddle in the vertical position, allow the system to come to rest, and take a second pair of density profiles. This procedure was repeated a number of times until the density profile started to deviate significantly (see below) from the initial value at which time the run was terminated. To our measurement accuracy, we could not detect any anomolous or preferential mixing near the top or bottom of the water column during a run and the change in the density profile appeared to occur over the entire depth – as figure 6 would suggest. For very large paddle amplitudes there was some visual indication of mixing around the paddle and in any such case the run was always aborted.

A check on the accuracy during a run was made by computing the total mass $\int_0^H \rho \, dz$ for each density profile, where H is the depth of the fluid. This statistic proved constant to an accuracy of better than $\pm 1\%$ over a run. For each profile, the potential energy per unit area was then computed as $\int_0^H \rho g z \, dz$. The data from all profiles were then plotted against the number of cycles and least-squares fit taken to determine the slope of the line – the potential energy gain per cycle – and finally multiplied by the horizontal cross-sectional area of the tank to determine the total increase in potential energy per cycle P. The regression coefficient from this least-

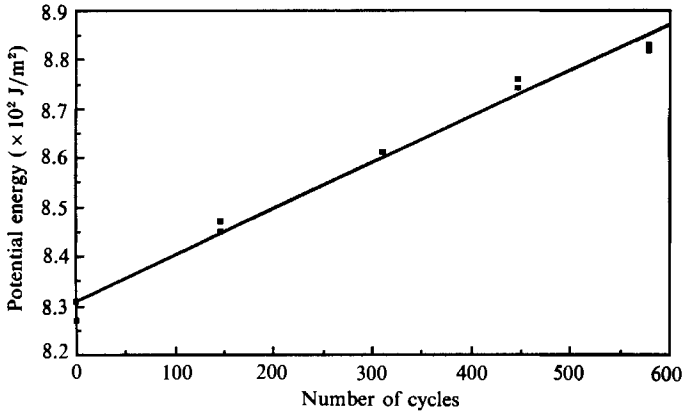

FIGURE 7. Potential energy of the water column per unit area as a function of the number of wave cycles.

squares fitting had values of 0.91 and 0.92 for the two worst cases and the remaining 10 runs (see figure 7) had regression coefficients of 0.98 ± 0.01.

As noted above, it took about 4 cycles after the commencement of paddle motion before the turbulent bottom boundary layer was established on the slope. Similarly, after the cessation of paddle motion it took a few cycles before the motion on the slope weakened to the point where the schlieren indicated that there was no further mixing along the bottom slope. These effects tend to balance one another and the technique of fitting a straight line to the data over several hundred cycles, as in figure 7 for example, thus yielded the best estimate of the increase in potential energy per cycle for steady forcing. Over the course of an entire run of several hundred cycles, the buoyancy frequency N does decrease slightly. While one should, therefore, also decrease the forcing frequency ω in order to exactly maintain critical conditions, in practice we kept ω constant and terminated the experiments when the ratio of ω/N had only varied by about 1–2% from the value at the start of the run. As figure 7 indicates, to the accuracy of our measurements the effect of this small shift from critical conditions in time was not detectable. We concluded that the accuracy of the measured potential energy gain per cycle P from these procedures was about $\pm 2\%$.

The work done by the paddle for each cycle is

$$W = \int_0^{2\pi/\omega} Fv \, \mathrm{d}t,$$

where ω is the forcing frequency, F the applied force and v the paddle velocity. In practice, $F = F_0 \sin(\omega t)$ and $v = (A_p \omega) \cos(\omega t - \phi)$, where A_p is the paddle displacement at the point of application of the force, and thus $W = F_0 A_p \pi \sin\theta$. The force F was measured directly by logging the output of the force transducer at 3.5 Hz and running the resultant signal through a fast Fourier transform in 512 element blocks to determine F_0. The force transducer was logged in a burst mode fashion about every 30 paddle cycles, for about 10 cycles. The accuracy of measurement of F_0 was about $\pm 3\%$, where the error bars represent one standard deviation about the mean from all estimates of F_0 in any one run. The amplitude A_p was fixed for each run, and in early runs the phase shift ϕ was measured by timing the difference between the peak in amplitude and force. Typical values of ϕ were around 135° with an error of $\pm 5\%$, where the error bars represent one standard deviation about the mean. In later runs,

a displacement transducer was connected to the paddle and the two transducers logged at 3.5 Hz in a burst mode fashion about every 30 paddle cycles for about 10 cycles as before. The displacement signal was differentiated to obtain velocity and the work then computed as before. In practice the two procedures yielded the same results and the measurement accuracy for W was about $\pm 8\%$.

The paddle created motion in the fluid by applying the boundary condition

$$\frac{\partial \psi}{\partial z} = A\left(\frac{2z}{H} - 1\right)\sin \omega t \quad \text{on } x = 0, \tag{2}$$

where ψ is the stream function, x the horizontal coordinate with origin at the paddle, z the vertical coordinate with origin at midheight, and A the paddle amplitude. The solution to the linearized wave equation

$$\nabla^2 \psi_{tt} + N^2 \psi_{xx} = 0 \tag{3}$$

subject to the boundary condition (2) and the no-flux boundary conditions

$$\frac{\partial \psi}{\partial x} = 0 \quad \text{on } z = 0, H \tag{4}$$

is (see Thorpe 1968)

$$\psi = \sum_{n=1}^{\infty} A_n \sin\left(\frac{n\pi z}{H}\right)\sin\left(k_n x - \omega t\right), \tag{5}$$

where the wavenumber k for mode n is given by

$$k_n^2 = \left(\frac{n\pi}{H}\right)^2\left(\frac{\omega^2}{N^2 - \omega^2}\right), \tag{6}$$

and the coefficients A_n are given by

$$A_n = \left(\frac{4A\omega H}{n^3\pi^3}\right)(1 - (-1)^n). \tag{7}$$

Only odd modes were thus present and their magnitude decayed rapidly with increasing n. Considering only the fundamental mode, therefore, the wave amplitude ζ and the wave steepness M for these mode 1 waves were given by

$$\zeta = \frac{A_1 k_1}{\omega} = \frac{8Ak_1 H}{\pi^3}, \quad M = \zeta k_1. \tag{8}$$

Of the total work or kinetic energy input, some was dissipated by viscous effects as the waves propagated from the paddle towards the sloping bottom. This viscous dissipation D is due to both internal dissipation and dissipation in the sidewall boundary layers. In general, the dissipation of energy per unit mass is given by (Lamb 1932, p. 580)

$$D_e = \rho_0 \nu \int_V \xi^2 \, \mathrm{d}V,$$

where V is the volume, and the vorticity $\xi = -\nabla^2 \psi$. An estimate of the dissipation in the tank can thus be obtained from the solutions in (5)–(7) above. In particular, the internal dissipation over one cycle D_{i}

$$D_{\mathrm{i}} = \rho_0 \nu\left[k_n^2 + \left(\frac{n\pi}{H}\right)^2\right]^2 \tfrac{1}{4} HLB\left(\frac{2\pi}{\omega}\right)\sum_{n=1}^{\infty} A_n^2, \tag{9}$$

where B is the tank breadth. To compute the dissipation in the sidewall boundary layers of the tank, we take the flow field as being described by a Stokes' flow of the form

$$u(n,t) = U_0[\cos\omega t - \mathrm{e}^{-\gamma n}\cos(\omega t - \gamma n)],$$

where $\gamma = (\omega/2\nu)^{\frac{1}{2}}$ and n is the coordinate normal to the wall. The dissipation on the sides over one cycle (cf. Schooley & Stewart 1963) was then

$$D_s = \rho_0 U_0^2 (\tfrac{1}{8}\nu\omega)^{\frac{1}{2}} A_s \left(\frac{2\pi}{\omega}\right). \tag{10}$$

Assuming that the dominant contribution comes from mode 1, for the sidewalls the velocity was $U_0^2 = \frac{1}{4}A_1^2[k_1^2 + (\pi/H)^2]$ and for the top and bottom walls $U_0^2 = \frac{1}{2}A_1^2[(\pi/H)^2]$. The areas in contact with the turbulent regions were negligibly small and the sidewall and top and bottom wall areas were thus 2.62 and 1.46 m^2, respectively. With these quantities, the total dissipation D was the sum of the estimates in (9) and (10). The former contribution is negligible, and the dissipation was dominated by the viscous dissipation in the wall boundary layers.

As these estimates of the dissipation assumed that the solution in (5)–(7) was applicable, a set of runs was conducted to examine the internal wave field in the interior of the tank. The observed wavenumbers were in accord with the predictions of this progressive wave solution and the observed wave amplitudes as a function of distance from the paddle are shown in figure 8 for three typical runs. The results are representative of the steady-state wave field and indicate that the reflection from the sloping boundary with its turbulent bottom boundary layer creates an amplitude-modulated progressive wave in the tank. For the purpose of the dissipation calculations above, we take a conservative approach and assume that the non-dimensionalized wave amplitude is 1 throughout the tank. While this is an approximation, as the results below indicate, the correction for the dissipation loss had only a small effect on the calculated mixing efficiencies.

Table 1 summarizes the results from 17 runs. The ratio of the gain in potential energy per cycle P to the work done per cycle W by the paddle on the fluid was defined as the overall mixing efficiency $\eta_0 = P/W$. Adding the errors involved in the calculation of P and W, the accuracy for η_0 was typically around 10% and specific values for each run are listed in the table. With the total viscous dissipation defined by D, the actual mixing efficiency η due to turbulent mixing by breaking internal waves on the bottom slope was therefore defined by $\eta = P/(W-D)$.

As a check on the estimated errors on the mixing efficiencies, the run with paddle amplitude $A = 3.68$ cm was repeated four times. The results from the four runs (table 1) yielded $\eta = 0.171, 0.179, 0.185$ and 0.194, respectively. Thus $\eta = 0.182 \pm 6\%$ encompasses all four estimates and the scatter is in good agreement with the estimated errors in table 1.

The overall mixing efficiency η_0 and the actual mixing η are plotted in figures 9(a) and 9(b), respectively, as a function of incident wave steepness M defined in (8). As discussed above, there was some uncertainty in the actual wave amplitude, and hence, in the wave steepness M and the implication was the incident wave steepness in figures 9(a) and 9(b) may in fact be a slight but consistent overestimate. Nevertheless, the figures both indicate a near-linear growth of the mixing efficiency with increasing wave steepness M until, for values of $M > 0.08$, there is the suggestion that the efficiencies are approaching an upper bound. The data are tightly

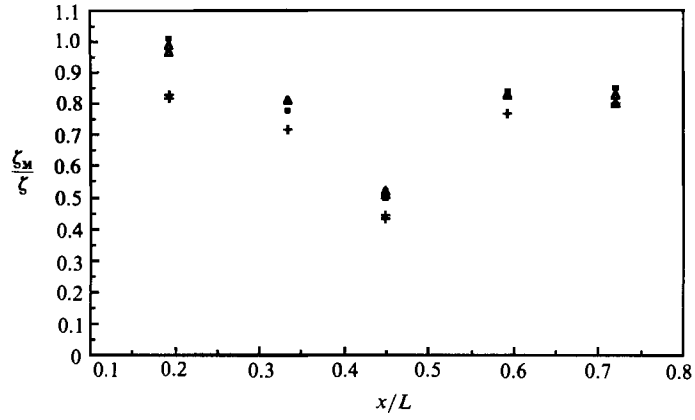

FIGURE 8. Non-dimensionalized measured wave amplitude ζ_M/ζ as a function of distance from the paddle, where $L = 150$ cm is the distance from the paddle to the base of the slope. Wave amplitudes ζ are 0.69 cm (+), 1.37 cm (Δ) and 1.71 cm (■).

Run	A cm	N_0 r/s	ω/N_0	P ($\times 10^4$) J	W ($\times 10^3$) J	η_0 ($\times 10^2$)	D ($\times 10^4$) J	η ($\times 10^2$)	Errors on η_0 and η ±%
65M	0.98	0.95	0.50	0	1.16	0	0.74	0	—
62M	1.23	0.96	0.50	0	0.96	0	1.08	0	—
45	1.23	0.94	0.50	0	1.11	0	1.68	0	—
66M	1.47	0.95	0.50	1.20	1.79	6.7	1.63	7.4	7
32	1.47	0.95	0.50	1.06	1.80	5.9	1.68	6.5	9
46	1.84	0.94	0.50	1.18	2.00	5.9	2.55	6.8	10
67M	2.02	0.92	0.50	2.26	2.25	10.0	3.03	11.6	7
26	2.21	1.01	0.50	2.77	2.96	9.3	4.06	12.0	12
28	2.94	0.83	0.50	3.61	3.13	11.5	5.52	14.0	13
30	2.94	0.92	0.50	4.00	3.99	10.0	6.33	11.9	10
37	3.31	0.96	0.50	6.83	5.18	13.2	8.54	15.8	11
43	3.68	0.83	0.50	5.82	4.00	14.5	8.48	18.5	10
42	3.68	0.91	0.50	7.59	5.21	14.6	9.76	17.9	10
36	3.68	0.98	0.50	10.40	6.44	16.1	10.80	19.4	11
41	3.68	1.00	0.50	8.47	6.06	14.0	11.20	17.1	11
38	3.98	0.89	0.50	8.47	5.37	15.8	10.80	19.7	11
40	4.29	0.85	0.50	8.69	5.92	14.7	11.70	18.3	12

TABLE 1. Summary of data from the experimental runs on mixing. The M after a run number indicates that the mesh was in place in the sloping boundary.

constrained and a linear least-squares fit to all the data in figure 9(*b*), for example, is $\eta = 2.18\,M - 0.014$ ($r^2 = 0.94$), *or roughly*

$$\eta \approx (2.2 \pm 0.1)\,M. \tag{11}$$

There is an additional way of looking at these mixing efficiencies which is enlightening and is in terms of the dependence of the mixing efficiency on the stability of the flow as expressed by an appropriate Richardson number. The mixing efficiency we have evaluated is a value representative of the entire turbulent

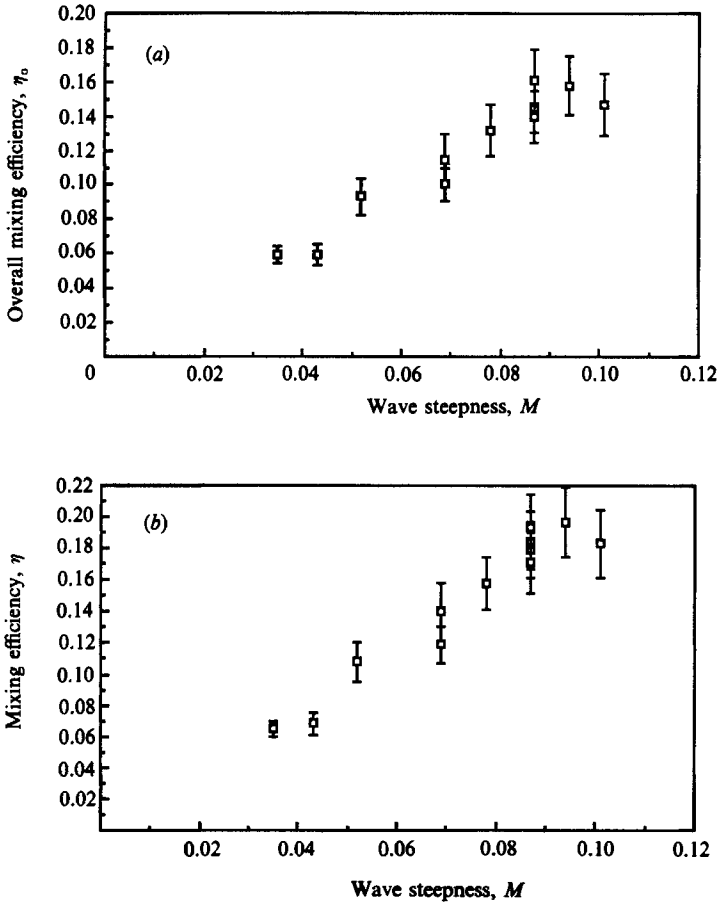

FIGURE 9. (*a*) Overall mixing efficiency η_o as a function of wave steepness M. (*b*) Mixing efficiency η as a function of wave steepness M.

boundary layer along the slope. We follow Turner (1973, p. 179), therefore, and take the appropriate overall Richardson number as

$$Ri = (N\delta/U)^2 \cos\theta, \tag{12}$$

The buoyancy frequency N is taken as the background stratification. The boundary-layer thickness δ is taken as the least-squares fit to the data in figure 4(*a*) (i.e. $\delta = 2.57\,\zeta + 3.5$ cm). Consistent with the definition in Turner (1973), U should be the mean speed parallel to the boundary over the boundary-layer thickness. Crudely, but consistently for all runs, we take this as $U = 0.37U_p$ where $U_p = 1.82\,\omega A + 0.61$ cm/s from figure 5. While this definition of Ri is specific to these experiments it is, nevertheless, very useful for comparing runs. The measured mixing efficiencies are plotted in figures 10(*a*) and 10(*b*) against the Richardson number defined in (12). Both plots indicate that the mixing efficiency is dependent on the stability of the flow and suggest the mixing efficiency is a maximum when $Ri \approx 18$. Note that owing to the strong shear within the boundary layer δ, the local value of the gradient Richardson number within δ will be considerably less. For larger values of Ri the efficiency decreases with increasing stability of the flow and most of our data clearly

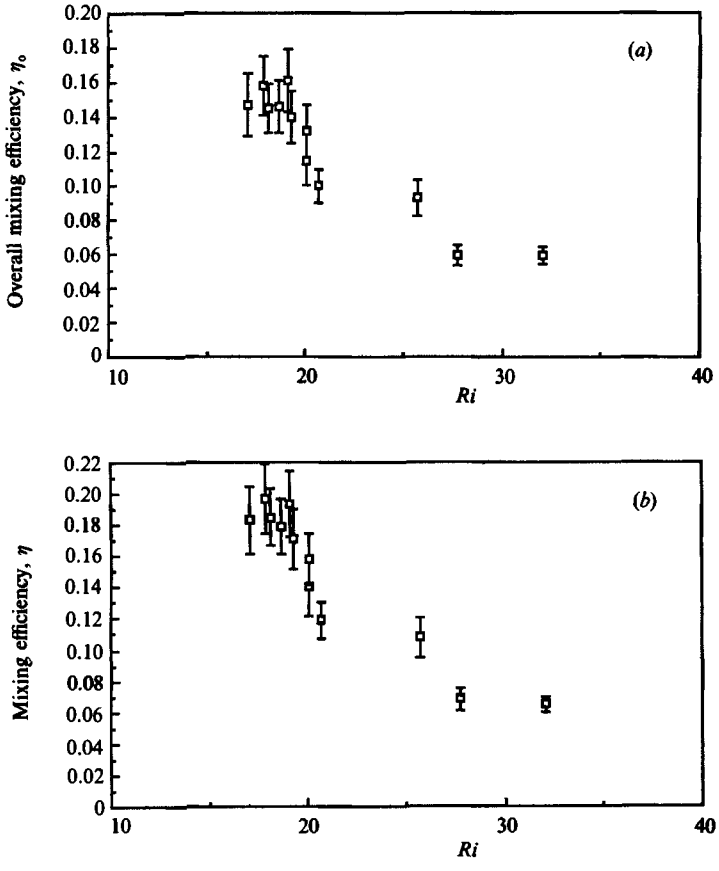

FIGURE 10. (*a*) Overall mixing efficiency η_0 as a function of the Richardson number Ri. (*b*) Mixing efficiency η as a function of Richardson number Ri.

lie in this range. Practical considerations do not allow us to run the experiment for smaller values of Ri than the range shown, but presumably the efficiency again decreases as Ri tends to zero – as Rohr & Van Atta (1987), for example, have observed in their water-tunnel experiments. While our data are limited in the range of Ri, they suggest that the form of the mixing efficiency versus Richardson number plot is one with a peak value at an intermediate value of Ri – as originally suggested by Linden (1979) and as observed in other mixing experiments with very different mixing mechanisms (eg. Linden 1980; Rohr, Itsweire & Van Atta 1984).

The data in figures 9 and 10 indicate that the peak value of the mixing efficiency is about 0.20. While the present experiment is unique, it is nevertheless interesting to compare this maximum efficiency with that obtained from other laboratory experiments with very different flow fields. Linden (1980) found a maximum efficiency of 0.12 from dropping grids through stratified fluids, McEwan (1983) a maximum of 0.36 with resonant internal wave breaking, Rohr *et al.* (1984) a maximum of 0.18 from grid-generated turbulence in a stratified water tunnel, and Pedersen & Jurgensen (1987) a value of 0.15 from a penetrative convection study. With the exception of the data of McEwan (1983), the maximum mixing efficiency observed in these experiments with very different flow fields therefore appears to be comparable with the value of 0.20 found in the present experiments.

5. Transition to mixing

In order for mixing to sustain a turbulent density flux, there must be a separation of overturning scales between the Ozmidov scale $L_O = (\epsilon/N^3)^{\frac{1}{2}}$, where buoyancy inhibits overturning, and the Kolmogorov scale $L_K = (\nu^3/\epsilon)^{\frac{1}{4}}$, where viscous effects damp any overturning motion. Thus, for a sustained turbulent density flux $L_O > L_K$ or $\epsilon > \nu N^2$. The transition value of the dissipation, defined by $\epsilon_{tr} = c\nu N^2$, where c is a constant to be determined, is thus the minimum value of the dissipation required to sustain a non-zero value of $\overline{\rho' w'}$ and is a fundamental parameter in mixing in stratified flows and of particular importance in the interpretation of turbulence measurements in the field (e.g. Imberger & Boashash 1986; Gregg 1987).

The dissipation rate may be measured for each of the runs in the present set of experiments. For any run we define the average dissipation rate over one wave cycle ϵ by

$$\epsilon = \frac{(W-D-P)}{MT}. \tag{13}$$

In (13), W is the measured work or kinetic energy input per cycle, D the total (laminar) dissipation by the waves as they propagated from the paddle to the ends of the tank, and P the measured increase in potential energy as the stratification weakened (see §4.2 above). T is the wave period and the mass of fluid in the turbulent boundary layers is $M = \rho(2LB\delta)$. In this expression L is the length of the sloping bottom (72 cm at each end of the tank), B the tank width (20 cm), and δ the thickness of the turbulent boundary layer measured perpendicular to the bottom. We confined ourselves to the case of critical waves since then the thickness δ is uniform along the slope and, from the schlieren observations in figure 4, was given by $\delta = 2.57\zeta + 3.5$ cm where ζ was the incident wave amplitude.

From figure 9 it is clear that as the wave amplitude decreased the efficiency also decreased. Eventually a point was reached where the mixing efficiency dropped to zero as the observed increase in potential energy per cycle P became zero. In figure 11, we plot the observed value of P versus the ratio $\epsilon/\nu N^2$. Above a value of $\epsilon_{tr}/\nu N^2 = 7$, we see a steady increase in P with increasing values of the ordinate.

The schlieren observations in §4.1 suggested that the mixing was more energetic during the phase of the wave cycle when the flow was upslope than during the phase of the wave cycle when the flow was downslope. While this suggests that the instantaneous value of the turbulent dissipation rate at a given location may be variable on timescales short compared with the wave period, the schlieren observations also indicated that the overturning motion was persistent over the wave cycle, implying the instantaneous value of the turbulent dissipation rate was above the transition value throughout the wave cycle. Note also that repeated profiling into the turbulent boundary layer indicated that the local value of N was within $\pm 10\%$ of the background stratification on any one profile, and we are thus justified in using the initial or background N here.

Examination of the form of (13) gives some indication of the accuracy of this estimate of ϵ_{tr}. In the numerator, the estimate of the work input W had an error of around $\pm 8\%$, the measured potential energy increase P had an error of around $\pm 2\%$, and the dissipation D was calculated analytically (see §4.2). The denominator in (13) contains two terms: the wave period T, which was measured precisely, and the total mass M in the boundary layer whose accuracy, in turn, was determined by the accuracy of the estimate of the turbulent-boundary-layer thickness δ from the data

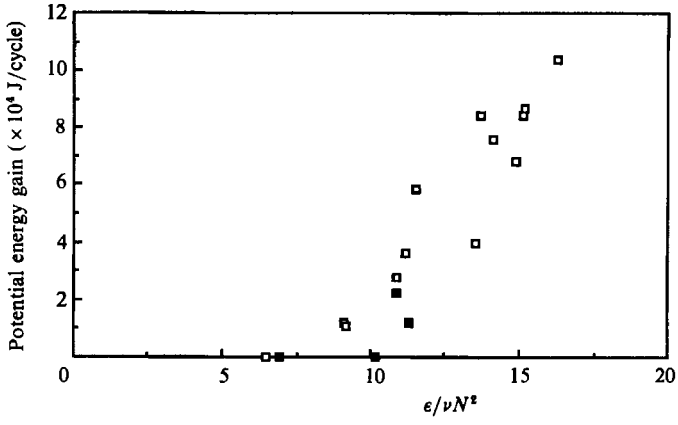

FIGURE 11. Increase in potential energy per wave cycle P as a function of $\epsilon/\nu N^2$. Data from runs with a smooth bottom (□) and for a bottom covered with a rough mesh (■).

presented in figure 4. This estimate of δ is probably accurate to about $\pm 10\%$. Thus the overall accuracy of an individual estimate of ϵ is about $\pm 20\%$. It is difficult to be more precise and for this reason we have not put error bars on the data in figure 11, although the scatter in the data suggests that these errors are reasonable and hence, the uncertainty in ϵ_{tr} is about $\pm 20\%$.

Stillinger, Helland & Van Atta (1983), Rohr (1985), and Itsweire, Helland and Van Atta (1986) reported a series of laboratory experiments where values of ϵ_{tr} were also measured. While these experiments were comparable with the present one in that they employed steady mixing, they were very different in character. Their experiments were done in a stratified water tunnel with a mean flow where turbulence was generated by placing a square bar mesh across the flow at the entrance to the control section. Rather than measure the increase of potential energy, local measurements of ϵ and $\overline{\rho' w'}$ were made downstream of the grid in order to find the value of ϵ_{tr} where $\overline{\rho' w'}$ decreased to zero. Itsweire *et al.* (1986) reported $\epsilon_{tr} = 21\nu N^2$ with a grid of mesh size $M = 3.81$ cm, Stillinger *et al.* (1983) (as corrected by Itsweire *et al.* 1986) found $\epsilon_{tr} = 15\nu N^2$ with a grid of mesh size $M = 1.905$ cm and Rohr (1985) found $\epsilon_{tr} = 16\nu N^2$ for the same mesh size and with a mean shear in the flow. These values of ϵ_{tr} are thus slightly larger than in our experiments, and also suggested some dependence on the overall Reynolds number of the flow.

To test this latter observation, we conducted four additional runs with a rough mesh installed along the sloping boundaries in order to alter the roughness Reynolds number. The roughness was an expanded aluminium mesh, of 9 mm by 29 mm, and when laid flush along the bottom slope the maximum height of the roughness elements were about 3 mm. The runs were confined to critical waves with $\omega = 0.5N$ in all cases. As in the case for smooth boundaries, a turbulent bottom boundary layer of uniform thickness formed along the bottom slope. The development and dynamics of the turbulent boundary layer along the sloping bottom were essentially the same as in the smooth-bottom case described in §4.1, although now the bottom boundary layer was slightly thicker: a least-squares fit to the data indicated the bottom-boundary-layer thickness, as determined from schlieren observations, was $\delta = 3.39\zeta + 1.54$ cm, where ζ was wave amplitude. With this boundary-layer thickness, the average dissipation was estimated in the same manner as before.

These results are marked differently and also shown in figure 11. The results

suggest that the transition to an active turbulent flow was occurring at a slightly higher value of $\epsilon_{tr}/\nu N^2 \approx 10$ for the rough boundary case. This trend of increasing ϵ_{tr} with an increase in the effective Reynolds number is thus consistent with the observations in the water-tunnel experiments. However, we have a only a limited number of data points and, since there was only a small change in the indicated value of ϵ_{tr}, this gives only weak support to the idea that the difference in the value of ϵ_{tr} is an effect of the Reynolds number. In the light of the comments above about the accuracy of the estimates of ϵ and to the accuracy of all the data in figure 11, it appears that the transition to a mixing flow with an observed increase in potential energy occurs when $\epsilon_{tr} = (8 \pm 2)\nu N^2$ for our experiments. This value of ϵ_{tr} is smaller than that found in the water-tunnel experiments and suggests that the exact value of ϵ_{tr} may depend on the actual mixing mechanism – a suggestion advanced by Itsweire *et al.* (1986). Nevertheless, it is important to note the value of the transition dissipation is $O(10)$ for all experiments.

6. Conclusions

The laboratory experiments described in this paper examined the mixing due to the breaking of internal waves in a continuously stratified fluid on a sloping boundary. Attention was confined to the case of critical waves when the slope of the group velocity vector equals the bottom slope.

In the experiments we observed that the initial wave breaking resembled that of a turbulent bore propagating up the slope. With the arrival of successive waves, a turbulent bottom boundary layer formed along the bottom slope providing that the Reynolds number $Re = \omega\zeta^2/\nu$ exceeded a critical value of 15–20, where ω was the wave frequency and ζ the wave amplitude. Turbulence was driven by a shear-flow instability and the steady-state boundary-layer thickness was $\delta \approx 5\zeta$.

Turbulent mixing was confined to the bottom boundary layer. The mixing efficiency was not constant, but was a function of the stability of the flow as measured by an overall Richardson number. The mixing efficiency had a maximum value of 0.20 at a finite value of the Richardson number – similar behaviour to observations of mixing in other very different flow fields. The mixing efficiency may also be viewed as a function of incident wave steepness.

The transition to mixing, defined as a turbulent flow with an increase in potential energy, was studied by computing the transition value of the dissipation rate ϵ_{tr} above which mixing occurred. In this context, ϵ_{tr} represents an averaged quantity over one wave cycle and was representative of the entire turbulent boundary layer. We find $\epsilon_{tr} = (8 \pm 2)\,\nu N^2$. The data also provided weak support for the dependence of ϵ_{tr} on the overall Reynolds number. Comparing the results to other experiments suggested that while the specific value of ϵ_{tr}, may be mechanism dependent, $\epsilon_{tr}/\nu N^2 = O(10)$ in all the available data sets.

The authors would like to thank our referees for many constructive comments on the manuscript. We would also like to thank Patrick Travers for his contributions to the design and construction of the laboratory facility and Ross Wylde-Browne for his assistance in the production of the rainbow filters and the photographs.

REFERENCES

ARMI, L. 1978 Some evidence for boundary mixing in the deep ocean. *J. Geophy. Res.* **83**, 1971–1979.

BAINES, P. G. 1986 Internal tides, internal waves, and near-inertial motions. In *Baroclinic Processes on Continental Shelves.* (ed. C. Moers). Coastal and Estuarine Science, vol. 3, pp. 19–31. AGU.

CACCHIONE, D. & WUNSCH, C. 1974 Experimental study of internal waves over a slope. *J. Fluid Mech.* **66**, 223–239.

ERIKSEN, C. C. 1985 Implications of ocean bottom reflection for internal wave spectra and mixing. *J. Phys. Oceanogr.* **15**, 1145–1156.

FORTUIN, J. 1960 Theory and application of two supplementary methods of constructing density gradient columns. *J. Polymer Sci.* **44**, 505–515.

GARRETT, C. 1979 Mixing in the ocean interior. *Dyn. Oceans Atmos.* **3**, 239–266.

GARRETT, C. & GILBERT, D. 1988 Estimates of vertical mixing by internal waves reflected off a sloping bottom. In *Small-Scale Turbulence and Mixing in the Ocean Proc. 19th Intl Liege Colloquim on Ocean Hydronamics (*ed. J. J. Nihoul & B. M. Jamart), pp. 405–424. Elsevier.

GREGG, M. C. 1987 Diapycnal mixing in the thermocline: A review. *J. Geophys. Res.* **92**, 5249–5286.

GREGG, M. C. & SANFORD, T. B. 1988 The dependence of turbulent dissipation on stratification in a diffusively stable thermocline. *J. Geophys. Res.* **93**, 12381–12392.

HOGG, N. G., BISCAYE, P., GARDNER, W. & SCHMITZ, W. J. 1982 On the transport and modification of Antarctic bottom water in the Vema Channel. *J. Mar. Res.* **40**, 231–263.

HOWES, W. L. 1984 Rainbow schlieren and its applications. *Appl Opt.* **23**, 2449–2460.

HOWES, W. L. 1985 Rainbow schlieren vs Mach–Zendler interferometer: a comparison. *Appl. Opt.* **24**, 816–822.

IMBERGER, J. & BOASHASH, B. 1986 Application of the Wigner–Ville distribution to temperature gradient microstructure: a new technique to study small scale variations. *J. Phys. Oceanogr.* **16**, 1997–2012.

ITSWEIRE, E. C., HELLAND, K. N. & VAN ATTA, C. W. 1986 The evolution of grid-generated turbulence in a stably stratified fluid. *J. Fluid Mech.* **162**, 299–338.

IVEY, G. N. 1987*a* The role of boundary mixing in the deep ocean. *J. Geophys. Res*, **92**, 11873–11878.

IVEY, G. N. 1987*b* Boundary mixing in a rotating, stratified fluid. *J. Fluid Mech.* **183**, 25–44.

IVEY, G. N. & CORCOS, G. M. 1982 Boundary mixing in a stratified fluid. *J. Fluid Mech.* **121**, 1–26.

LAMB, H. H. 1932 *Hydrodynamics* (6th edn). Dover, 738 pp.

LINDEN, P. F. 1979 Mixing in stratified fluids. *Geophys. Astrophys. Fluid Dyn.* **13**, 3–23.

LINDEN, P. F. 1980 Mixing across a density interface produced by grid turbulence. *J. Fluid Mech.* **100**, 691–703.

MCEWAN, A. D. 1983 Internal mixing in stratified fluids. *J. Fluid Mech.* **128**, 59–80.

MOUM, J. N. & OSBORN, T. R. 1986 Mixing in the main thermocline. *J. Phys. Oceanogr.* **16**, 1250–1259.

MUNK, W. 1966 Abyssal recipes. *Deep Sea Res.* **13**, 707–730.

PHILLIPS, O. M., SHYU, J.-H. & SALMUN, H. 1986 An experiment on boundary mixing: mean circulation and transport rates. *J. Fluid Mech.* **173**, 473–499.

PEDERSEN, F. B. & JURGENSEN, C. 1987 Laboratory experiments on entrainment due to free convection. *Third Intl. Symp. on Stratified Flows, Cal. Instit. Tech., Pasadena, Calif.*, vol. **2**, A4, pp. 11.

ROHR, J. J. 1985 An experimental study of evolving turbulence in uniform mean shear flows with and without stable stratification. Ph.D thesis, University of California, San Diego.

ROHR, J. J., ITSWEIRE, E. C. & VAN ATTA, C. W. 1984 Mixing efficiency in stably-stratified decaying turbulence. *Geophys. Astrophys. Fluid Dyn.* **29**, 221–236.

ROHR, J. J. & VAN ATTA, C. W. 1987 Mixing efficiency in stably stratified growing turbulence. *J. Geophys. Res.* **92**, 5481–5488.

SAUNDERS, P. M. 1987 Flow through Discovery Gap. *J. Phys. Oceanogr.* **17**, 632–643.

SCHOOLEY, A. H. & STEWART, R. W. 1963 Experiments with a self-propelled body submerged in a fluid with a vertical density gradient. *J. Fluid Mech.* **15**, 83–96.

STILLINGER, D. C., HELLAND, K. N. & VAN ATTA, C. W. 1983 Experiments on the transition of homogeneous turbulence to internal waves in a stratified fluid. *J. Fluid Mech.* **131**, 91–122.

THORPE, S. A. 1968 On the shape of progressive internal waves. *Proc. R. Soc. Lond.* A **263**, 563–614.

THORPE, S. A. & HAINES, A. P. 1987 Appendix to On the the reflection of a train of finite-amplitude gravity waves from a uniform slope. *J. Fluid Mech.* **178**, 279–302.

TURNER, J. S. 1973 *Buoyancy Effects in Fluids.* Cambridge University Press.